Section 4. Helioseismology and Asteroseismology

https://doi.org/10.1017/S1743921324000176 Published online by Cambridge University Press

https://doi.org/10.1017/S1743921324000176 Published online by Cambridge University Press

Invited talks

https://doi.org/10.1017/S1743921324000176 Published online by Cambridge University Press

https://doi.org/10.1017/S1743921324000176 Published online by Cambridge University Press

Dynamics of Solar and Stellar Convection Zones and Atmospheres
Proceedings IAU Symposium No. 365, 2024
A. V. Getling & L. L. Kitchatinov, eds.
doi:10.1017/S1743921324000176

Recent Progress in Time–Distance Helioseismology: Meridional Circulation, Far-side Imaging, and Sunquakes

Ruizhu Chen and Junwei Zhao

W. W. Hansen Experimental Physics Laboratory, Stanford University, Stanford, CA, USA
email: rzchen@stanford.edu

Abstract. Time–distance helioseismology uses solar surface Doppler observations to measure areas that are not directly observable, such as solar interior, far side, and sunquake sources. In this work, we briefly review recent advancements in time–distance helioseismology, focusing on meridional circulation measurements, far-side imaging, and sunquakes. Solar deep meridional flows are crucial for understanding the dynamics of the solar interior, but precise measurements of these flows are challenging. This review explores recent developments in this area, particularly highlighting new findings related to systematic effects that have long challenged meridional circulation determination. We also review recent progress in solar far-side imaging, which is useful in improving space weather forecasting. Recent developments in far-side imaging using time–distance techniques and Deep Learning are introduced. Additionally, we review a new approach in sunquake reconstruction by incorporating observation-based Green's functions constructed by time–distance helioseismology.

Keywords. Sun: helioseismology, Sun: interior, Sun: magnetic fields, Sun: oscillations

1. Introduction

Helioseismology utilizes solar surface Doppler observations to investigate regions of the Sun that are beyond direct observation, such as the solar interior and the far side. Time–distance helioseismology, a local-scale method within this field, studies these regions by tracking the propagation of acoustic waves and analyzing their travel times over specific distances. The subtle changes in wave travel times reflect the physical conditions along their paths, allowing for the inferences of various physical quantities. This technique enables researchers to measure solar subsurface structures, examine variations in wave-speed perturbations and flows in sunspots, and physical condition down to the base of the convection zone. In this paper, we will review recent developments using time–distance helioseismology, focusing on three topics: solar meridional circulation, far-side imaging, and sunquakes.

The Sun's meridional circulation is a global-scale interior flow of solar material from the solar equator toward the poles and back in the Sun's meridional plane. It is a crucial component for understanding the solar dynamo and interior dynamics, facilitating the transport of magnetic flux and the redistribution of angular momentum (e.g., Wang *et al.* 1989; Miesch 2005; Upton & Hathaway 2014a,b; Featherstone & Miesch 2015). Additionally, it has been reported to be associated with the length and strength of solar cycles (Hathaway & Rightmire 2010; Dikpati *et al.* 2010). Surface meridional flows have been extensively measured in various studies, consistently reporting a poleward flow on the order of $10-20$ m s^{-1}. This has been achieved through methods such as surface

© The Author(s), 2024. Published by Cambridge University Press on behalf of International Astronomical Union.

https://doi.org/10.1017/S1743921324000176 Published online by Cambridge University Press

Doppler measurements (e.g. Duvall 1979; Hathaway 1996), surface feature tracking (e.g. Howard & Gilman 1986; Komm *et al.* 1993; Švanda *et al.* 2007), time–distance helioseismology (e.g. Giles *et al.* 1997; Zhao & Kosovichev 2004), ring-diagram analysis (e.g. González Hernández *et al.* 1999; Haber *et al.* 2000), and Fourier–Legendre analysis (e.g. Braun & Fan 1998; Roth *et al.* 2016). However, determining deep meridional flow proves to be notoriously difficult, resulting in inconsistencies across previous studies. Questions regarding the number of circulation cells and the depth of the return flow still remain open. Most measurements of deep meridional circulation employ the time–distance helioseismology method. In Section 2, we'll provide a brief review of these studies, with an emphasis on recent developments about the associated systematic effects that have posed challenges in the meridional-flow determination.

The Solar far side is crucial for effective space weather forecasting. Given the Sun's rotation period of about 27 days, phenomena developing on the far side take time to rotate into view on the Earth side. Accurate solar wind modeling requires boundary conditions of full solar surface spanning 360°, and missing half of the surface diminishes predictive capabilities. For a few years, direct observations of the far side in extreme ultraviolet (EUV) were available through the Solar Terrestrial Relations Observatory (*STEREO*; Howard *et al.* 2008), with two spacecraft orbiting the Sun ahead and behind Earth. With *STEREO* currently positioned back on the Earth side, the solar far side is beyond direct observation. The recent launch of the *Solar Orbiter* (*SO*; Müller *et al.* 2013) has reintroduced direct far-side observation, albeit sporadically on a shorter time scale. On the other hand, through a technique known as helioseismic far-side imaging, helioseismologists can utilize near-side Doppler observations to map the far side's surface and identify large active regions (ARs). This method offers valuable insights into the far side in near-real-time when direct observation is unavailable. Section 3 will provide a brief review of developments in helioseismic far-side imaging, with a particular focus on recent improvements with time–distance methods and their integration with deep learning.

Sunquakes manifest as enhancements in photospheric oscillatory power triggered by solar flares, with photospheric helioseismic waves becoming visible approximately 10-30 minutes after the flare onset in the surrounding area. Proposed mechanisms to initiate sunquakes are diverse, with suggestions that they may be excited by sudden photospheric pressure perturbations caused by shock waves (Kosovichev & Zharkova 1998; Kosovichev 2007; Zharkova & Zharkov 2007), photospheric heating (Donea *et al.* 2006; Lindsey & Donea 2008), or Alfvén-wave heating (Russell & Fletcher 2013; Reep & Russell 2016). Other studies also propose that the Lorentz force drives sunquakes (Hudson *et al.* 2008; Fisher *et al.* 2012). However, these mechanisms fall short in explaining why not all flares result in sunquakes. Despite the tendency for sunquakes to occur during strong flares, only a fraction of such flares induce sunquakes, and intriguingly, even weak flares can occasionally cause sunquakes (Buitrago–Casas *et al.* 2015; Sharykin & Kosovichev 2020). In Section 4, we introduce a recent study that aims to address this question. This work utilizes time–distance methods to derive observation-based Green's functions, which are then incorporated into sunquake reconstructions.

2. Meridional Circulation

2.1. *Inconsistent Measurements of Meridional Circulation*

An early measurement of solar deep meridional flow was conducted by Giles (2000) using time–distance method, employing data from the *Solar and Heliospheric Observatory* / Michelson Doppler Imager (*SOHO*/MDI; (Scherrer *et al.* 1995)). Poleward flows were identified spanning nearly the entire convection zone, and an equator-ward flow was inferred near the base of the convection zone after applying a mass-conservation

https://doi.org/10.1017/S1743921324000176 Published online by Cambridge University Press

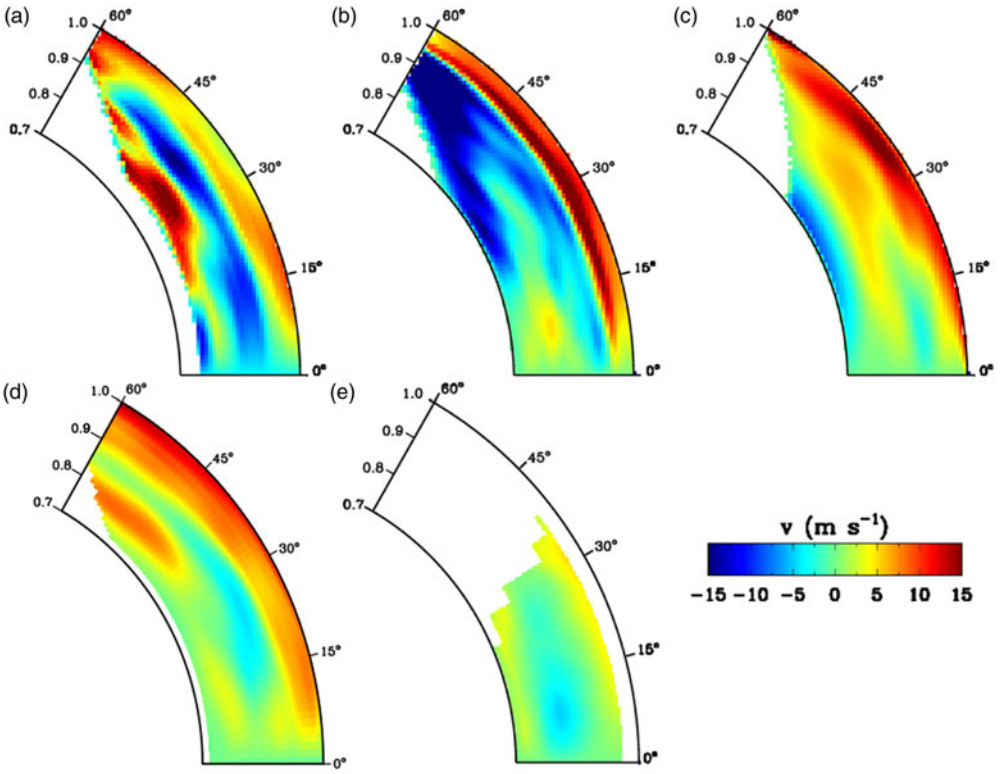

Figure 1. Comparison of hemispherically symmetrized meridional circulation for selected results by time–distance method, from (a) Zhao *et al.* (2013), (b) Kholikov *et al.* (2014); Jackiewicz *et al.* (2015), (c) Rajaguru & Antia (2015), (d) Chen & Zhao (2017), and (e) Lin & Chou (2018). Adapted from Figure 1.8 of Chen (2019).

constraint, forming an single-cell circulation. This result was achieved long before the recognition of a systematic effect, identified later as the center-to-limb (CtoL) effect, which significantly affects deep flow inferences by introducing an additional systematic signal (Zhao *et al.* 2012). It is found that the CtoL effect increases when going deeper and from the disk center to the limb, reaching magnitudes as large as 5–10 times of the flow-caused signal. By empirically removing this effect, Zhao *et al.* (2013) successfully detected the equator-ward flow using first two years of data from *Solar Dynamics Observatory* / Helioseismic and Magnetic Imager (*SDO*/HMI; Scherrer *et al.* 2012; Schou *et al.* 2012), revealing a shallow return flow between 0.82 $R_\odot$ and 0.91 $R_\odot$, below which the meridional flow exhibites poleward again (Figure 1(a)). The resulting flow profile indicates a double-cell circulation pattern.

Subsequent studies affirmed the presence of the center-to-limb (CtoL) effect across various instruments. Employing the same effect-removal strategy and similar measurement techniques, these investigations also identified the return flow but at varying depths, resulting in different meridional flow profiles. Utilizing GONG data, Kholikov *et al.* (2014) and Jackiewicz *et al.* (2015) observed a shallow return flow at a depth similar to Zhao *et al.* (2013), yet reported no additional poleward flow in deeper layers (Figure 1(b)). Analyzing 4 years of HMI observations, Rajaguru & Antia (2015) found the equatorward flow only beneath 0.77 $R_\odot$, suggesting a single-cell circulation (Figure 1(c)). Utilizing MDI data, Liang & Chou (2015b) and Lin & Chou (2018) reported a 3-layer meridional flow profile during two solar minima, with a return flow in the middle of the convection zone,

https://doi.org/10.1017/S1743921324000176 Published online by Cambridge University Press

Table 1. Comparison of procedures in different meridional circulation measurements with time–distance method

Authors	Instruments	Observation Time	Filtering	Magnetic Masking	CtoL Removal Method	Sensitivity Kernels	Inversion method	Circulation
Zhao *et al.* (2012)	HMI	2010 May - 2012 April	running difference	None	EW measurement proxy	Ray path approximation	Rregularized Least Squares (RLS)	double-cell
Kholikov *et al.* (2014) Jackiewicz *et al.* (2015)	GONG	652 selected days in 2004–2012	phase-speed filter	None	EW measurement proxy	Ray path approximation	Subtractive Optimally Localized Average (SOLA)	single-cell
Böning *et al.* (2017)						Born approximation	refined SOLA	single- or multiple-cell
Rajaguru & Antia (2015)	HMI	2010 May - 2014 April	running difference	None	EW measurement proxy	Ray path approximation	stream function RLS with built-in mass conservation	single-cell
Rajaguru & Antia (2020)		2010 May - 2021 April						single-cell (3 mHz) double-cell (4 mHz)
Mandal *et al.* (2018)		2010 May - 2016 April				Born approximation		single-cell
Chen & Zhao (2017)	HMI	2010 May - 2017 April	running difference	Yes	Least-square disentangle	Ray path approximation	RLS	double-cell
Liang & Chou (2015b) Lin & Chou (2018)	MDI	1996 May - 2010 November	High-pass > 1.5mHz	Yes	EW measurement proxy	Ray path approximation	SOLA	double-cell at solar minima
Gizon *et al.* (2020)	MDI & GONG	1996 May - 2011 April & 2001 August - 2019 April		Yes	EW measurement proxy	Born approximation	stream function RLS with mass conservation	single-cell

Adapted and Updated from Table 1 of Chen (2019)

indicating a double-cell circulation (Figure 1(e)). However, during the solar maximum, the circulation pattern became more complex. Gizon *et al.* (2020) conducted extensive measurements using HMI, MDI, and GONG data. They had to exclude HMI results due to an unclear systematic issue causing severe North–South asymmetry in their HMI measurements. Their results, using MDI and GONG data, reported a single-cell meridional circulation throughout Solar Cycles 23 and 24.

In all these investigations, a uniform strategy for removing the center-to-limb (CtoL) effect was employed. This approach uese East–West measurements along the equator as a proxy for the CtoL effect, which is then subtracted from North–South measurements along the central meridian. The assumption made was that the CtoL effect is consistent along both the equator and the central meridian. To examine this assumption, Chen & Zhao (2017) devised a comprehensive method for measurements along all disk-radial directions, subsequently solving the CtoL effect through a least-square method. Their study confirmed that the CtoL effect is isotropic relative to the azimuthal angle (within certain limitations). Moreover, they were able to disentangle the CtoL effect from the meridional-flow-induced travel-time shifts in a more robust manner. The outcomes of their investigation revealed a double-cell circulation profile (Figure 1(d)).

The exact cause of the inconsistencies among these studies remains elusive. Multiple differences exist in the detailed measurement procedures, as summarized in Table 1. Due to space constraints, this review will not go through all of them. However, it is believed that the discrepancies likely stem from variations in the flow inversion process and the CtoL effect removal procedures. Notably, Rajaguru & Antia (2015), Mandal *et al.* (2018), and Gizon *et al.* (2020) incorporated a strict mass conservation in their inversion using regularized least squares (RLS) methods. All three reported a deep return flow, indicating a single-cell circulation pattern. The incorporation of the mass conservation constraint may contribute to the systematic differences in the inverted circulation profile. On the other hand, challenges arise in effectively removing the systematic CtoL effect. In deep regions, the CtoL effect could be 5-10 times larger than the flow-induced signals. Therefore, a small error in the CtoL effect removal can lead to a substantial change in the inverted flow profile. However, thoroughly evaluating whether the CtoL effect has been effectively removed by these empirical methods poses a significant challenge.

https://doi.org/10.1017/S1743921324000176 Published online by Cambridge University Press

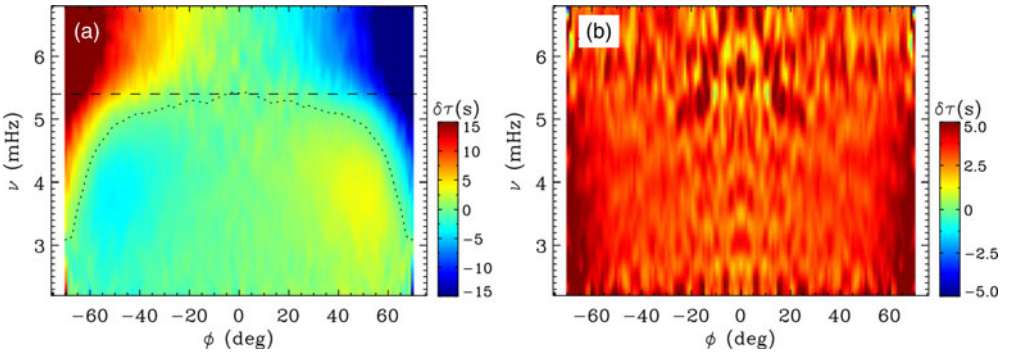

Figure 2. (a)Profile of the CtoL effect for an effective travel distance of 21.°6. The dotted line is a smoothed contour at value of 0, and the dashed line represents the frequency of 5.4 mHz. Adapted from Figure 7(a) of Chen & Zhao (2018). (b)Rotation-induced travel-time shifts, displayed as a function of disk-centric distance and frequency for a travel-distance of 14.°4. Adapted from Figure 11(a) of Chen & Zhao (2018).

A recent discovery by Chen & Zhao (2018) offers a potential means to assess the efficacy of systematic effect removal and enhances our understanding of the physics behind the CtoL effect. Notably, the CtoL effect exhibits a significant frequency dependence, changing signs at around 5.4 mHz. Furthermore, the frequency-dependent behavior varies markedly with disk-centric distance but not much with travel distance (Figure 2(a)). In contrast, travel-time shifts induced by flows show little frequency dependence (Figure 2(b)). This pronounced difference provides an opportunity to enhance the disentanglement of the CtoL effect from meridional-flow measurements. The findings of this study introduce a new dimension of information to the meridional flow problem. Ideally, flows measured and inverted across different frequencies should be invariant, allowing the examination of CtoL effect removal by comparing results at multiple frequencies. Later, Rajaguru & Antia (2020) conducted a frequency-dependent meridional flow measurement by applying frequency filters to their measurements. Their results revealed a single-cell circulation profile at 3 mHz and a double-cell profile at 4 mHz, suggesting unresolved issues in the measurement process.

Similar frequency-dependent travel-time aymmetries were also observed in measuring travel times between different atmospheric heights using HMI line-core and continuum intensities (Zhao & Chen 2020). In fact, the Center-to-Limb (CtoL) effect occurs between different disk-centric locations, suggesting that the cause of the CtoL effect likely originates from the different line-formation heights..

To investigate this scenario, Zhao *et al.* (2022) employed a set of high-spectral-resolution, high-cadence observational data from the *Interferometric BI-dimensional Spectrometer (IBIS)* installed at the *Dunn Solar Telescope*. This instrument observes the same spectral line as HMI (Fe I λ6173.3 $\mathring{A}$). Dopplergrams at different atmospheric heights were constructed using the bisector method. The evanescent waves above the photosphere were found carrying nonnegligible phase shifts that cannot be explained by flows. Moreover, these phase shifts also exhibit significant frequency dependence. Figure 3 compares the frequency dependence of the CtoL effect in Panel (a) with that of the non-zero phase shifts between multiple heights in Panel (b). Although not quantitatively close, they exhibit qualitatively similar dependencies on frequency. Both change from positive to negative at a certain frequency, and their magnitudes increase with the atmospheric height difference. The cause of the phase shifts between different heights is not immediately clear, but it is likely related to the non-adiabatic nature of

https://doi.org/10.1017/S1743921324000176 Published online by Cambridge University Press

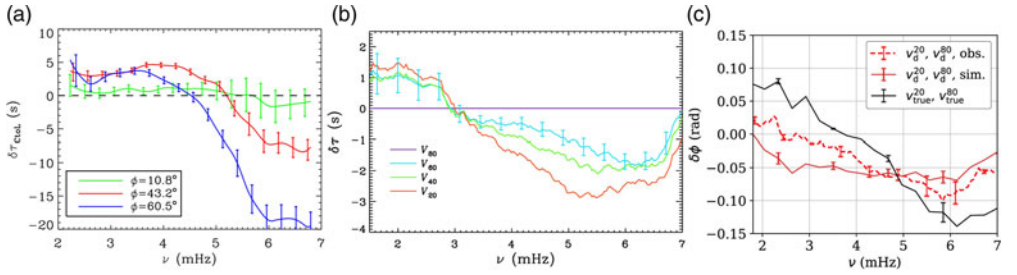

Figure 3. (a)The CtoL effect as functions of frequency at selected disk-centric locations. Adapted from Figure 9(a) of Chen & Zhao (2018). (b) Time shifts measured between IBIS Depplergrams derived at 20%, 40%, 60%, and 80% intensity level (higher to lower atmospheric heights) relative to that of 80% intensity level (lowest height derived), displayed as functions of frequency. Adapted from Figure 5(b) of Zhao *et al.* (2022). (c) Phase differences at the disk center as functions of frequency for Doppler velocities derived from the bisector method for IBIS data (dashed curves), derived from simulation data (solid), and true velocities (black solid curves). Adapted from Figure 8(a) of Waidele *et al.* (2023).

the atmosphere and complicated radiative transfer above the photosphere. This finding also alerts helioseismologists about systematic effects in helioseismic measurements when using oscillatory signals observed at different atmospheric heights, not limited to meridional flow measurements by time–distance helioseismology.

To further investigate the physics behind these unexpected phase shifts, Waidele *et al.* (2023) conducted similar measurements of phase shifts on a simulated, fully radiative, and convective atmosphere from which the Fe I λ6173.3 $\mathring{A}$ line is synthesized. Doppler velocities at different atmospheric heights were calculated using the bisector of the spectral line. Subsequently, phase shifts were calculated between these Doppler velocities and also between the true velocities at corresponding heights in the simulation. Nonnegligible phase shifts that vary with frequency were measured in both cases. However, their magnitudes are not close, and both deviate from the observations (Figure 3(c)). All these frequency-dependent phase shifts pose challenges to the interpretation of helioseismic measurements but also provide more observational constraints on understanding the physics behind various systematics.

In summary, current studies on solar meridional circulation involve ongoing efforts to refine measurements, address systematic effects, and explore new approaches for understanding the complex systematics. Challenges persist, but these studies contribute valuable insights and constraints, pushing forward the boundaries of our knowledge about meridional flow.

3. Far-Side Imaging

3.1. *Helioseismic Far-Side Imaging*

The first successful far-side active region detection was made by Lindsey & Braun (2000a) using the Doppler-velocity data from MDI by employing helioseismic holography method Lindsey & Braun (2000b)). The method was later expanded to achieve entire far-side coverage (Braun & Lindsey 2001; Lindsey & Braun 2017; Yang *et al.* 2023a). Time–distance methods were also developed to detect far-side ARs (Duvall *et al.* 2000) by tracking waves propagating from the near side to the far side and then back to the near side. These waves get reflected multiple times on the solar surfaces, carrying information that can be used to map the far-side surface conditions. Zhao (2007) developed this method by designing and measuring different wave-propagation schemes, achieving better

https://doi.org/10.1017/S1743921324000176 Published online by Cambridge University Press

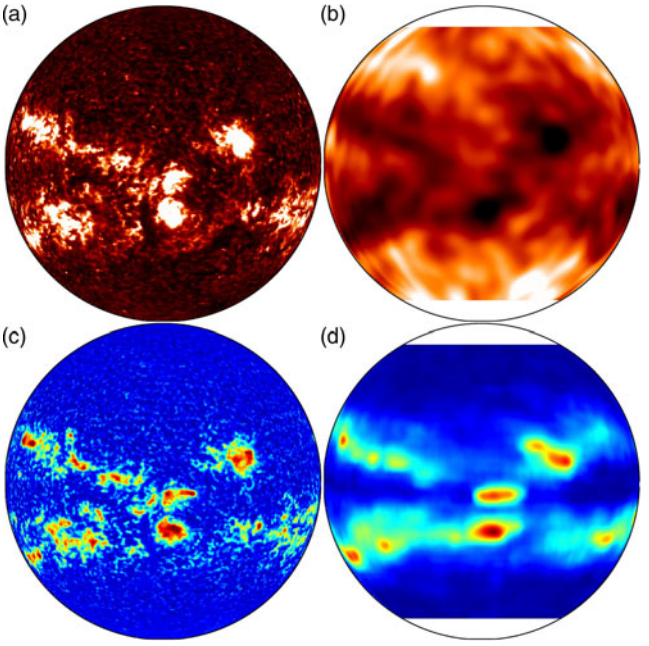

Figure 4. (a) Observed EUV 304 Å map merged from *STEREO* A & B spacecraft data; (b) Helioseismic far-side image obtained from the new timedistance far-side imaging codes (Zhao *et al.* 2019); (c) Far-side unsigned magnetic-flux map generated using *STEREO* observations and the machine-learned EUV-to-magnetic mapping relation (Chen *et al.* 2022); (d) Far-side magnetic-flux map generated using helioseismic far-side images and the machine-learned acoustic-to-magnetic mapping relation (Chen *et al.* 2022).

performance by superimposing the results of multiple schemes. Initially, Zhao (2007) developed codes for calculating 4-skip and 5-skip schemes, and Ilonidis *et al.* (2009) added 3-skip ones for improvements.

With *STEREO*'s direct far-side observations, far-side active regions (ARs) can be monitored in EUV channels, enabling a systematic evaluation of the performance of helioseismic far-side imaging techniques. In a series of articles, Liewer *et al.* (2012, 2014, 2017) compared *STEREO* 304 Å images with helioseismic holography far-side images and found that 95% of the helioseismically-detected far-side ARs correspond to an EUV brightening area.

Recently, Zhao *et al.* (2019) improved the time–distance far-side imaging technique by introducing additional wave propagating schemes, resulting in a total of 14 sets of measurements. This significantlly elevated the sensitivities and reliability of their time–distance far-side imaging tool. Through an examination of helioseismic maps generated using near-side HMI Dopplergrams and *STEREO*'s direct far-side EUV observation, the study demonstrated that 97.3% of helioseismically detected far-side ARs larger than a certain size were found to correlate with an observed region exhibiting strong EUV brightening. Furthermore, 85.7% of ARs observed by *STEREO*, larger than a certain size, proved detectable in the helioseismic images. Such remarkable performance holds great potential to improve space weather forecasting. Figure 4 showcases the *STEREO*-observed EUV image (Panel a) and the helioseismic far-side map (Panel b) of the Sun's far side on 2014 Mar 13. A pipeline has been established to generate such helioseismic far-side maps in near-real time.

https://doi.org/10.1017/S1743921324000176 Published online by Cambridge University Press

3.2. *Incorporating Machine Learning techniques.*

While significant progress has been achieved in the field of helioseismic far-fide imaging, there remains one particular gap to fill. The helioseismic far-side maps provide information in terms of travel-time shifts, not magnetic fields. However, solar wind modeling demands global magnetic field data for a high quality in space weather forecasting (Nitta & DeRosa 2008; Schrijver & Title 2011). To fulfill this need, modelers have developed flux-transport models (e.g., Schrijver & DeRosa 2003; Upton & Hathaway 2014b) to approximate the far-side magnetic field by migrating the magnetic field observed on the near side towards the far side with decay. However, such methods are incapable of predicting the growth or new emergence of active regions.

A recent study by Chen *et al.* (2022) aimed to address this problem using machine learning. This work developed an approach to calibrate far-side acoustic images into far-side unsigned magnetic-flux maps using *STEREO* EUV observations as a bridge. Two machine-learning models were trained to achieve this goal. The first model converts EUV 304 Å maps to unsigned magnetic flux maps, trained using 9 years of near-side observations by *SDO*/AIA and *SDO*/HMI. This model transforms the *STEREO* EUV 304 Å images into far-side unsigned magnetic-flux proxies (with certain calibrations between *STEREO* and AIA EUV observations). Using these (*STEREO*-based) far-side magnetic-flux proxies as targets, the second model was trained to convert helioseismic far-side images into (acoustic-based) magnetic-flux maps. Once trained, the second model can produce future acoustic-based unsigned magnetic-flux maps in near-real-time solely based on near-side Doppler observations. Figure 4(c) shows their *STEREO*-based far-side magnetic flux on this date (as an intermediate data product), and Figure 4(d) shows their final acoustic-based unsigned magnetic-flux map. Although being low-resolution, these acoustic-based far-side magnetic-flux maps can provide useful information about the far side's magnetic fields when direct observation is unavailable.

This is not the only work leveraging the power of machine learning to improve helioseismic products. In fact, machine learning has been applied in multiple aspects to enhance the detection of far-side ARs and estimating magnetic fields. Felipe & Asensio Ramos (2019) and Broock *et al.* (2021) trained a machine-learning model that compared the far-side EUV Images and the helioseismic-holography images before these helioseismic images were routinely overlapped for 5 days to enhance the signal-to-noise ratio. This approach resulted in a higher confidence in detecting smaller far-side ARs that might otherwise be neglected. Additionally, signed magnetic fields were obtained by authors using deep-learning methods from *SDO*/AIA EUV maps (e.g., Kim *et al.* 2019), and in following studies, from *STEREO* EUV maps as well (Jeong *et al.* 2020; Alshehhi 2020). However, considering the low resolution and large uncertainty of helioseismic far-side imaging, generating signed magnetic fields is challenging, as acoustic signals exhibit no sensitivity to the polarity of the magnetic field.

3.3. *Direct Far-side Magnetogram Observation from SO.*

The recent launch of the *Solar Orbiter* (*SO*; (Müller *et al.* 2013)) has reintroduced direct far-side observation. In particular, the Polarimetric and Helioseismic Imager (PHI) on board *SO* provides line-of-sight magnetograms of the far side during the cruise and the early science phase of the mission (Solanki *et al.* 2020). This marks the first direct observation of far-side magnetic fields, offering valuable data for calibrating far-side magnetic field proxies. With access to a limited sample of 6 ARs on 3 magnetograms, (Yang *et al.* 2023b) established an empirical relation between helioseismic far-side measurements (Yang *et al.* 2023a) and directly observed magnetic flux. Future observations will enable calibration on a larger sample, holding the potential to significantly enhance solar far-side imaging.

https://doi.org/10.1017/S1743921324000176 Published online by Cambridge University Press

4. Sunquakes

Sunquakes often occur in active regions following strong flares. Although the sunquake regions are usually observed, the velocity data are often corrupted due to irregular spectrum lines in high temperature and violent dynamics following the flares. Sunquakes' velocity fields are often reconstructed and measured by the helioseismic holography method (Lindsey & Braun 1997, 2000a). This approach essentially reverses the expanding sunquake ripples backward to the sunquake initiation time and location to reconstruct the sunquake source (Donea *et al.* 2000), measure the sunquake energy (Zharkov *et al.* 2013; Sharykin *et al.* 2017), or probe into the submerged sources (Lindsey *et al.* 2020). The reversal of waves is achieved by deconvolution with a Green's function, typically calculated theoretically using a standard quiet-Sun model. However, albeit being noise-free, theoretical Green's functions carry biases in determining the sunquake initiation time, as sunquakes often occur in active regions rather than the quiet regions where the Green's function is calculated.

Recently, Chen & Zhao (2021) employed time–distance methods to derive observation-based Green's functions for waves propagating outside sunspot umbra, penumbra, and surrounding quiet regions. These observation-based Green's functions were then integrated into the helioseismic holography method to reconstruct the sunquake velocity fields. This approach is expected to provide more precise time determinations. With this enhancement, Chen & Zhao (2021) investigated the relationship between flares and sunquakes, aiming to answer the question of why some flares trigger sunquakes while others do not.

Their hypothesis introduces the consideration of photospheric background oscillation as a contributing factor for sunquakes, a factor often overlooked in previous studies. They propose that during the impulsive phase of a flare, when the flare's impulse influences the photosphere through shock waves, energetic particles, or downward Lorentz Force, a sunquake is more likely to occur if the background oscillation at the flare footpoint oscillates downward in the same direction as the impulse from above. This alignment enhances the background oscillation to a detectable level against the ambient background oscillations. To test this hypothesis, they analyzed 60 strong flares in Solar Cycle 24, examining the background oscillatory velocity at the sunquake sources during the flares' impulsive phases. Given the short time periods of solar oscillations, precise time determination of the sunquake's velocity field, as mentioned earlier, is crucial for this investigation. Their findings indicate that out of the 60 studied flares, 24 are helioseismically active, resulting in a total of 41 sunquake events (in either frequency range). In the $3-5$ mHz frequency band, 80.6% of the 31 sunquakes exhibit average downward velocities during the flares' impulsive phases, and in the $5-7$ mHz frequency band, 86.8% of the 38 sunquakes have net downward velocities. This consistency supports their hypothesis that sunquakes are more likely to occur when the downward flare impact strengthens a pre-existing downward background oscillation. Despite supporting statistics, it is acknowledged that the proposed background oscillation serves as a selection rule that restricts the chance for a sunquake to occur, but does not explain how or when a flare triggers a sunquake in the first place. Nevertheless, this work may provide new insights to understand the puzzling sunquake triggering mechanisms.

5. Conclusion

In conclusion, recent advancements in time–distance helioseismology have significantly improved our understanding of various solar phenomena. These developments include refining measurements, addressing systematic effects, and exploring novel approaches to overcome challenges in the field. Studies on solar meridional circulation have revealed discrepancies in flow profiles, prompting investigations into the removal of systematic

https://doi.org/10.1017/S1743921324000176 Published online by Cambridge University Press

effects like the CtoL effect. Frequency-dependent observations have provided insights into the nature of the CtoL effect, introducing new dimensions to meridional flow studies. Machine learning applications have enhanced the detection of far-side active regions and the estimation of magnetic fields, opening avenues for improved space weather forecasting. Additionally, the integration of time–distance-derived Green's functions has enhanced the precision of time determination for sunquakes using holography methods. This improvement contributes to our understanding of the potential influence of photospheric background oscillations on sunquake triggering during solar flares. Despite these advancements, challenges and gaps persist, underscoring the need for continued research to unravel the complexities of solar dynamics and improve the accuracy of helioseismic measurements.

Acknowledgements. *SDO* is a NASA mission, and HMI project is supported by NASA contract NAS5-02139 to Stanford University. R.C. and J.Z. are partly supported by NASA DRIVE Center COFFIES grant 80NSSC22M0162.

References

Alshehhi, R. 2020, *Proceedings of the IEEE/CVF Conference on Computer Vision and Pattern Recognition Workshops*, 204–205
Böning, V. G. A., Roth, M., Jackiewicz, J., & Kholikov, S. 2017, *Astrophys. J.*, 845, 2
Braun, D. C., & Fan, Y. 1998, *Astrophys. J. Letters*, 508, L105
Braun, D. C. & Lindsey, C. 2001, *Astrophys. J. Lett.*, 560, L189.
Broock, E. G., Felipe, T., Asensio Ramos, A. 2021, *A&A*, 652, A132
Buitrago–Casas, J. C., Martínez Oliveros, J. C., Lindsey, C., *et al.* 2015, *Solar Phys.*, 290, 3151
Chen, R., 2019, PhD dissertation, Stanford University
Chen, R., & Zhao, J. 2017, *Astrophys. J.*, 849, 144
Chen, R., & Zhao, J. 2018, *Astrophys. J.*, 853(2), 161
Chen, R. & Zhao, J. 2021, *Astrophys. J.*, 908, 182
Chen, R., Zhao, J., Hess Webber, S., *et al.* 2022, *Astrophys. J.*, 941, 197
Dikpati, M., Gilman, P. A., de Toma, G., & Ulrich, R. K. 2010, *Geophys. Res. Lett.*, 37, L14107
Donea, A.-C., Besliu–Ionescu, D., Cally, P. S., Lindsey, C., & Zharkova, V. V. 2006, *Solar Phys.*, 239, 113
Donea, A.-C., Lindsey, C., & Braun, D. C. 2000, *Solar Phys.*, 192, 321
Duvall, T. L., Jr. 1979, *Solar Phys.*, 63, 3
Duvall, T. L., Kosovichev, A. G., & Scherrer, P. H. 2000, *AAS/Solar Physics Division Meeting* #31
Featherstone, N. A., & Miesch, M. S. 2015, *Astrophys. J.*, 804, 67
Felipe, T., Asensio Ramos, A. 2019, *A&A*, 632, A82
Fisher, G. H., Bercik, D. J., Welsch, B. T., & Hudson, H. S. 2012, *Solar Phys.*, 277, 59
Giles, P. M. 2000, PhD dissertation, Stanford University
Giles, P. M., *et al.* 1997, *Nature*,
Gizon, L., Cameron, R. H., Pourabdian, M., *et al.* 2020, *Science*, 368, 1469
González Hernández, I., *et al.* 1999, *Astrophys. J. Lett.*, 510, L153
Haber, D. A., Hindman, B. W., Toomre, J., *et al.* 2000, *Solar Phys.*, 192, 335
Hathaway, D. H. 1996, *Astrophys. J.*, 460, 1027
Hathaway, D. H., & Rightmire, L. 2010, *Science*, 327, 1350
Howard, R., & Gilman, P. A. 1986, *Astrophys. J.*, 307, 389
Howard, R. A., Moses, J. D., Vourlidas, A., *et al.* 2008, *Space Sci. Rev.*, 136, 67
Hudson, H. S., Fisher, G. H., & Welsch, B. T. 2008, in ASP Conf. Ser. 383, Subsurface and Atmospheric Influences on Solar Activity, ed. R. Howe,
Ilonidis, S., Zhao J., & Hartlep, T. 2009, *Solar Phys.*., 258, 181
Jackiewicz, J., Serebryanskiy, A., & Kholikov, S. 2015, *Astrophys. J.*, 805, 133
Jeong, H.-J., Moon, Y.-J., Park, E., *et al.* 2020, *Astrophys. J. Lett.*, 903, L25

https://doi.org/10.1017/S1743921324000176 Published online by Cambridge University Press

Kim, T., Park, E., Lee, H., *et al.* 2019, *Nature Astron*, 3, 397
Komm, R. W., Howard, R. F., & Harvey, J. W. 1993, *Solar Physics*, 147, 207
Kholikov, S., Serebryanskiy, A., & Jackiewicz, J. 2014, *Astrophys. J.*, 784, 145
Kosovichev, A. G. 2007, *Astrophys. J. Lett.*, 670, L65
Kosovichev, A. G., & Zharkova, V. V. 1998, *Nature*, 393, 317
Liang, Z.-C., & Chou, D.-Y. 2015, *Astrophys. J.*, 809, 150
Liewer, P. C., González Hernández, I., Hall, J. R., Lindsey, C., & Lin, X. 2014, *Solar Phys.*., 289, 3617
Liewer, P. C., González Hernández, I., Hall, J. R., Thompson, W. T., & Misrak, A. 2012, *Solar Phys.*., 281, 3
Liewer, P. C., Qiu, J., & Lindsey, C. 2017, *Solar Phys.*., 292, 146
Lindsey, C., & Braun, D. C. 1997, *Astrophys. J. Lett.*, 485, 895
Lin, C.-H., & Chou, D.-Y. 2018, *Astrophys. J.*, 860, 48
Lindsey, C., & Braun, D. C. 2000a, *Science*, 287, 5459
Lindsey, C., & Braun, D. C. 2000b, *Solar Phys.*., 192, 261
Lindsey, C., & Braun, D. C. 2017, *Space Weather*, 15, 761
Lindsey, C., & Donea, A.-C. 2008, *Solar Phys.*, 251, 627
Lindsey, C., Buitrago–Casas, J. C., Martínez Oliveros, J. C., *et al.* 2020, *Astrophys. J. Lett.*, 901, L9
Mandal, K., Hanasoge, S. M., Rajaguru, S. P., & Antia, H. M. 2018, *Astrophys. J.*, 863, 39
Miesch, M. S. 2005, Living Rev. *Solar Phys.*., 2, 1
Müller, D., Marsden, R. G., St. Cyr, O. C., *et al.* 2013, *Astrophys. J.*, 285, 25
Nitta, N. V., & DeRosa, M. L. 2008, *Astrophys. J. Lett.*, 673, L207
Rajaguru, S. P., & Antia, H. M. 2015, *Astrophys. J.*, 813, 114
Rajaguru, S. P. & Antia, H. M. 2020, *Dynamics of the Sun and Stars; Honoring the Life and Work of Michael J. Thompson*, 57, 107.
Reep, J. W., & Russell, A. J. B. 2016, *Astrophys. J. Lett.*, 818, L20
Roth, M., Doerr, H.-P., & Hartlep, T. 2016, *A&A*, 592, A106
Russell, A. J. B., & Fletcher, L. 2013, *Astrophys. J.*, 765, 81
Scherrer, P. H., Bogart, R. S., Bush, R. I., *et al.* 1995, *Solar Phys.*, 162, 129
Scherrer, P. H., Schou, J., Bush, R. I., et al. 2012, *Solar Phys.*, 275, 207
Schou, J., Scherrer, P. H., Bush, R. I., et al. 2012, *Solar Phys.*, 275, 229
Schrijver, C. J., & DeRosa, M. L. 2003, *Solar Phys.*, 212, 165
Schrijver, C. J., & Title, A. M. 2011, *J. Geophys. Res.*, 116, A04108
Sharykin, I. N. & Kosovichev, A. G. 2020, *Astrophys. J.*, 895, 76
Sharykin, I. N., Kosovichev, A. G., Sadykov, V. M., Zimovets, I. V., & Myshyakov, I. I. 2017, *Astrophys. J.*, 843, 67
Solanki, S. K., del Toro Iniesta, J. C., Woch, J., *et al.* 2020, *A&A*, 642, A11
Švanda, M., Zhao, J., & Kosovichev, A. G. 2007, *Solar Phys.*, 241, 27
Upton, L., & Hathaway, D. H. 2014a, *Astrophys. J.*, 780, 5
Upton, L., & Hathaway, D. H. 2014b, *Astrophys. J.*, 792, 142
Waidele, M., Zhao, J., & Kitiashvili, I. N. 2023, *Astrophys. J.*, 949, 99.
Wang, Y.-M., Nash, A. G., & Sheeley, N. R., Jr. 1989, *Science*, 245, 712
Yang, D., Gizon, L., Barucq, H., *et al.* 2023, *A&A*, 674, A183
Yang, D., Gizon, L., & Barucq, H. 2023a, *A&A*, 669, A89
Yang, D., Gizon, L., Barucq, H., *et al.* 2023b, *A&A*, 674, A183
Zhao, J., & Kosovichev, A. G. 2004, *Astrophys. J.*, 603, 776
Zhao, J., Bogart, R. S., Kosovichev, A. G., Duvall, T. L., Jr. 2013, *Astrophys. J. Lett.*, 774, L29
Zhao, J. & Chen, R. 2020, *Dynamics of the Sun and Stars; Honoring the Life and Work of Michael J. Thompson*, 57, 123.
Zhao, J. 2007, *Astrophys. J. Lett.*, 664, L139
Zhao, J., Hing, D., Chen, R., & Hess Webber, S. 2019, *Astrophys. J.*, 887, 216

https://doi.org/10.1017/S1743921324000176 Published online by Cambridge University Press

Zhao, J., Nagashima, K., Bogart, R. S., Kosovichev, A. G., Duvall, T. L., Jr. 2012, *Astrophys. J. Lett.*, 749, L5
Zhao, J., Rajaguru, S. P., & Chen, R. 2022, *Astrophys. J.*, 933, 109
Zharkov, S., Green, L. M., Matthews, S. A., & Zharkova, V. V. 2013, *Solar Phys.*, 284, 315
Zharkova, V. V., & Zharkov, S. I. 2007, *Astrophys. J.*, 664, 573

https://doi.org/10.1017/S1743921324000176 Published online by Cambridge University Press